Supporting Information

Song et al. 10.1073/pnas.1214739110

SI Materials and Methods

Crystallization and Structure Solution of the Dermcidin Peptide. The dermcidin peptide sequence (Fig. S1) was synthesized by the company Peptide2.0 (www.peptide2.com) to yield a product of >97% purity. For crystallization, the peptide was dissolved in 10 mM Hepes at a concentration of 50 mg/mL (~10 mM final concentration). Crystallization drops were prepared by mixing 400 nL of the peptide solution with the same amount of reservoir, and drops were incubated by vapor diffusion (sitting drops) under a variety of different conditions (800 conditions from Qiagen screens). Two conditions, both of which contained Zn-acetate, yielded crystals suitable for X-ray diffraction analysis. Crystals for X-ray diffraction were taken from a drop containing 0.2 M $Zn(ac)_2$, 0.1 M Na-cacodylate, 18% (wt/vol) PEG8000 at pH 6.5. Crystals were taken from the mother liquor and flash-frozen in liquid nitrogen without adding cryoprotectant. Data were collected at the Swiss Light Source, beamline PXII at 100 K and 20 eV above the theoretical Zn-edge (9.658 keV). Three-hundred sixty 1° images were collected at 2% beam intensity to generate a highly redundant dataset for single anomalous dispersion data processing. Diffraction data were processed with XDS/XSCALE (1). The structure was solved with the PHENIX program package (2) with Phaser (3) for heavy atom detection and Resolve (4) for initial solvent flattening. Solvent flattening was repeated by Pirate of the CCP4 suite (5) and a model with 85% completeness was built with Buccaneer (6). The final model was obtained after several rounds of manual rebuilding and refinement with Coot (7), REFMAC (8), and PHENIX (2). The structural geometry of all ligand structures was verified with Whatcheck (9); values are given in Table S1. Crystal structure images were generated with Pymol (Schrodinger). Sequence alignment of human dermcidin (DCD) (Fig. S1) was performed against sequences deposited to the current EXPASY (10) sequence database. Sequences similar to DCD were extracted with a PSI-BLAST (11) search. In addition, the secondary structure was predicted with PSIPRED (12).

Electrophysiology. Giant unilamellar vesicles (GUVs) were prepared by the electroformation method (13–15). A lipid mixture composed of diphytanoyl phosphatidylcholine (DPhPC)/cholesterol (9:1) dissolved in chloroform at a concentration of 10 mM (6.25 μL) was deposited on indium-tin-oxide (ITO) coated cover slides and allowed to dry. Two slides were connected to form a sealed chamber electrically connected to a voltage generator (33210A; Agilent Technologies). The lipid was rehydrated in approximately 2 mL 1 M sorbitol and GUV formation was carried out by application of a 3-V peak-to-peak AC voltage at a frequency of 5 Hz for 2 h at 20 °C.

A freestanding membrane was prepared by spreading a GUV on an aperture with a size of a few micrometers in diameter in a borosilicate chip (Port-a-Patch; Nanion Technologies). Two microliters of the GUV-containing solution were added to 6-μL buffer (1 M NaCl, 5 mM Hepes, pH 7.1) and a GUV was gently sucked onto the aperture by application of 15–40-mbar negative pressure. Spontaneous spreading of the GUV on the surface gave rise to a solvent-free membrane with resistances in the GΩ range.

After successful membrane formation, 50 μL of buffer were added and varying amounts of DCD-1L stock solution (100 μM) were added at a DC bias of 100 mV. Current traces were recorded with an Axopatch 200B amplifier (Axon Instruments). The analog output signals were filtered with a low-pass four-pole Bessel filter of 1 kHz and subsequently digitized by an A/D converter (Digidata 1322; Axon Instruments). The sampling rate was 50 kHz. Data evaluation was performed with the pClamp 9 software package (Axon Instruments).

Solid-State NMR Spectroscopy. Samples for solid-state NMR spectroscopy were prepared by dissolving 4 mg of peptide and ~30 mg of lipid in TFE/water 50/50 vol/vol. Where appropriate $ZnCl_2$ was added in five- to ten-fold molar excess over the peptide. The solutions were mixed and carefully applied onto 20 ultra-thin cover glasses (6 × 11 mm; Paul Marienfeld) as described previously (16). Care was taken to remove all organic solvent in high vacuum. Thereafter, the samples were equilibrated at 93% relative humidity for several days.

An alternative preparation method consisted in mixing only the lipid in organic solvent and forming a dry film by evaporating the solvent and exposure to high vacuum (16, 17). Then 0.2 mL of water was added and a transparent vesicular suspension was prepared (five freeze/thaw cycles between liquid nitrogen and 310 K water bath). Thereafter 2 mg of peptide and 62 μg of $ZnCl_2$ were codissolved in 100 μL of water and added to the membrane vesicles, vortexed, and incubated for 4 h. The mixed lipid/peptide vesicles were applied onto glass plates, dried in air overnight, and equilibrated at 93% relative humidity.

Solid-state NMR spectra were recorded on a Bruker Avance wide-bore NMR spectrometer operating at 9.4 T. A commercial double-resonance solid-state NMR probe modified with flattened coils of dimensions 15 × 4 × 9 mm was used. Proton-decoupled ^{15}N solid-state NMR spectra were acquired using a cross-polarization sequence and processed as described previously (18). The temperature was 310 K for 1-palmitoyl-2-oleoyl-*sn*-glycero-3-phosphoethanolamine (POPE)/1-palmitoyl-2-oleoyl-*sn*-glycero-3-phospho(1′-*rac*-glycerol) (POPG) and 295 K for 1-palmitoyl-2-oleoyl-*sn*-glycero-3-phosphocholine (POPC) and DPhPC/cholesterol 9:1 membranes. NH_4Cl (40.0 ppm) was used as an external reference corresponding to 0 ppm for liquid NH_3. An exponential apodization function corresponding to a line broadening of 50 Hz was applied before Fourier transformation.

Deuterium solid-state NMR spectra were recorded using a quadrupolar echo pulse sequence (19). The spectra were referenced relative to ^2H_2O (0 Hz). An exponential apodization function corresponding to a line broadening of 500 Hz (for the $^2H_3$-peptide) or 30 Hz (for chain deuterated lipids) was applied before Fourier transformation. The deuterium order parameters are analyzed following reference (20).

To verify the alignment of the lipids, proton-decoupled ^{31}P solid-state NMR spectra were recorded using a Hahn-echo pulse sequence as described previously (18) and referenced relative to 85% phosphoric acid (0 ppm).

Calculation of Orientational Restraints from the Solid-State NMR Spectra. To evaluate the peptide orientations that agree with the experimental spectra, a coordinate system was defined, with the tilt angle being the angle between the long axis of the helix and the membrane normal, and a pitch angle between membrane normal and the line within the arbitrary plane of peptide helical wheel projection (see Fig. S2*B* for angle definition). The calculations were performed using the ^{15}N chemical shift main tensor elements for glycine (44, 65, 211) ppm (21) to agree with an isotropic chemical shift of 106.7 ppm and 74 kHz for the maximum quadrupolar splitting for the alanine ^2H_3C-group at room temperature (22). The coordinates of DCD were from pdb:2ymk. By successively changing the tilt and pitch angles in (50 × 50 steps), the 3D topological space was systematically

screened and the corresponding ^{15}N chemical shift and quadrupolar splitting calculated (19). The restriction plot was calculated using azimuthal fluctuations of 18° Gaussian distribution and wobbling motions of 10°, similar to those which have been observed for other in-plane amphipathic helical peptides (e.g., refs. 23, 24). Contour plots mark the angular restrictions that agree with the experimental results.

Molecular Dynamics Simulations. All molecular dynamics (MD) simulations were performed with the GROMACS package, version 4.5 (25, 26) in combination with the CHARMM36 force field (27). Unless otherwise stated, the simulation temperature was 310 K. The protein, lipids, and water/ions were coupled separately to a temperature bath with the v-rescale method with a time constant of 0.1 ps (28). Short-range electrostatics were calculated with a cutoff of 1.3 nm. Long-range electrostatics were treated with the particle-mesh Ewald method (29, 30). Short-range Van der Waals (VdW) interactions were calculated explicitly up to a distance of 0.8 nm, beyond which a switch function was used to smoothly switch off the VdW interactions to reach zero at 1.2 nm. All bonds were constrained with the LINCS method (31). The time step was 2 fs for all-atom MD simulations and 4 fs for simulations with the virtual site model for hydrogen atoms (32), respectively.

The crystal structure of the DCD hexamer, as described in this study, was used to generate the initial configuration for our MD simulations. Specifically, the protein and six Zn^{2+} ions at the monomeric interfaces of the DCD oligomer were taken from the crystal structure, which was then embedded into a mixed bilayer of palmitoyloleoyl-phosphatidylethanolamine and palmitoyloleoylphosphatidylglycerol (POPE/POPG; 3:1) lipids, which resembles the composition of the bacterial cytoplasmic membrane (33). To test the tilting of DCD in various bilayer environments, additional simulations were carried out in dimyristoyl phosphatidylcholine (DMPC), dipalmitoyl phosphatidylcholine (DPPC), distearoyl phosphatidylcholine (DSPC), and diarachidonoyl phosphatidylcholine (DAPC) lipid bilayers. All membranes were generated with CHARMM-GUI (34).

The POPE/POPG bilayer consisted of 72 POPE and 24 POPG molecules in each bilayer leaflet, solvated by 13,938 TIP3P water molecules (35). Also, 82 Na^+ and 38 Cl^- ions were added to the simulation system resulting in an ionic strength of about 150 mM. The POPE/POPG lipids were first energy-minimized for 5,000 steps with the steepest descent algorithm, then equilibrated in an NVT ensemble at 310 K for 500 ps, while position restraints were applied (1,000 $kJ{\cdot}mol^{-1}{\cdot}nm^{-2}$) on the lipid heavy atoms. Subsequently, the system was further equilibrated without any restraints under semi-isotropic Berendsen pressure coupling (36). The reference pressure was set to 1 bar and the pressure coupling time constant was 1.0 ps. After ~1 ns of simulation in the NPT ensemble, the area per lipid reached about 0.615 nm^2. This configuration was adopted for additional 15 ns of NPAT simulation to further equilibrate the system. The GROMACS utility g_membed (37) was used to insert DCD into the lipid bilayer. By comparing the lateral pressures to those of pure lipids, we found that by removing nine lipid molecules, the differences between the lateral pressures of DCD-embedded and pure systems are smallest. Therefore, approximately nine lipid molecules were removed in each leaflet before insertion of the DCD oligomer. To test convergence, we used three different initial configurations of the lipid bilayer in our MD simulations by taking frames at various points of the equilibration simulation (taken at 13, 14, and 15 ns from the above lipids equilibration simulation). The antimicrobial peptide (AMP) assembled structure was thus inserted into three different membrane microenvironments. The adoption of three independent initial simulation systems can reduce possible bias on the simulation results arising from the initial system setup. One of the resulting single-bilayer simulation systems is shown in Fig. S5 *A* and *B*.

Starting from the three independent systems described above, we first performed 5,000 steps of steepest descent energy minimization, then 10 ns of NPAT equilibration simulations with the heavy atoms of the protein and Zn^{2+} position restrained (1,000 $kJ{\cdot}mol^{-1}{\cdot}nm^{-2}$). These equilibration simulations allowed water molecules to fill the interior of the DCD oligomer. Monitoring of the number of water molecules showed that it no longer increased after 7.5 ns. Subsequently, 250-ns simulations were performed for all of the three systems under NPAT conditions. In addition, we performed three corresponding simulations without any Zn^{2+} in the system to investigate the importance of Zn^{2+} for the stability of the X-ray structure.

To study whether the oligomer is ion conductive, we used the computational electrophysiology method (38). Structures were taken from the three single-patch simulations at 100 ns and the systems were duplicated in the Y direction. The virtual-site model was used for peptides and lipids (32). A transmembrane electric field was generated by sustaining a slight imbalance of ions in the two compartments thus formed during the simulation by ion exchanges. This ionic imbalance evoked an electrostatic potential gradient across the two bilayers of ± 200–800 mV in multiple simulations, as determined by double integration of Poisson's equation (38). Under these conditions, six independent 200-ns production simulations were performed with a time step of 4 fs in the NPAT ensemble. The simulation system of the double-bilayer setup is shown in Fig. S5*C*.

To run simulations under conditions similar to our electrophysiological experiments, we also carried out computational electrophysiology simulations, in which 506 Cl^- and 594 Na^+ ions were included in the double-patch system, which resulted in an ion concentration of ~1 M. Here again, an equal number of Cl^- ions were included in the two compartments, and a small difference of Na^+ ions between compartment I and II was sustained during the simulation, which generated transmembrane potentials fluctuating in the range from ~20 to 300 mV. Subsequently, five independent simulations were performed to monitor ion permeation.

Altogether, we performed five independent double-patch simulations with 1M NaCl (200 ns each), six independent double-patch simulations with 150 mM NaCl (200 ns each), four single-patch simulations with various lipids (>250 ns each), three independent single-patch simulations (250 ns each), and three independent single-patch simulations in the absence of Zn^{2+} (200 ns each). Simulation images were generated with Pymol (Schrodinger).

Pore Size Analysis. To good approximation, the conductance of membrane channels is proportional to their channel cross-sectional area; i.e., it varies with the square of the difference of the pore radii (39). Due to the fact that the channel is composed of units of antiparallel dermcidin dimers, it is reasonable to assume that channel-forming oligomers would consist of an even number of 4, 6, 8, etc., peptides. By using the peptide–peptide docking software m-Zdock (40), which is specialized for generating symmetrical pores, we find that (*i*) tetrameric assemblies are not capable of forming a pore, and (*ii*) peptide octamers with their hydrophobic face toward the membrane would have a pore diameter of about ~11 Å. According to our calculations, this pore size would lead to a conductance above 0.5 nS. This value is more than five times higher than that found in our experiments. Higher-order oligomers could be expected to have a further increased conductance. Hence, lower- or higher-order dermcidin channels are not a likely explanation for our experimentally measured channel currents.

1. Kabsch W (2010) Integration, scaling, space-group assignment and post-refinement. *Acta Crystallogr D Biol Crystallogr* 66(Pt 2):133–144.
2. Adams PD, et al. (2011) The Phenix software for automated determination of macromolecular structures. *Methods* 55(1):94–106.
3. Read RJ, McCoy AJ (2011) Using SAD data in Phaser. *Acta Crystallogr D Biol Crystallogr* 67(Pt 4):338–344.
4. Zwart PH, et al. (2008) Automated structure solution with the PHENIX suite. *Methods Mol Biol* 426:419–435.
5. Winn MD, et al. (2011) Overview of the CCP4 suite and current developments. *Acta Crystallogr D Biol Crystallogr* 67(Pt 4):235–242.
6. Cowtan K (2006) The Buccaneer software for automated model building. 1. Tracing protein chains. *Acta Crystallogr D Biol Crystallogr* 62(Pt 9):1002–1011.
7. Emsley P, Lohkamp B, Scott WG, Cowtan K (2010) Features and development of Coot. *Acta Crystallogr D Biol Crystallogr* 66(Pt 4):486–501.
8. Murshudov GN, et al. (2011) REFMAC5 for the refinement of macromolecular crystal structures. *Acta Crystallogr D Biol Crystallogr* 67(Pt 4):355–367.
9. Schwede T, Kopp J, Guex N, Peitsch MC (2003) SWISS-MODEL: An automated protein homology-modeling server. *Nucleic Acids Res* 31(13):3381–3385.
10. Gasteiger E, et al. (2003) ExPASy: The proteomics server for in-depth protein knowledge and analysis. *Nucleic Acids Res* 31(13):3784–3788.
11. Altschul SF, Gish W, Miller W, Myers EW, Lipman DJ (1990) Basic local alignment search tool. *J Mol Biol* 215(3):403–410.
12. Jones DT (1999) Protein secondary structure prediction based on position-specific scoring matrices. *J Mol Biol* 292(2):195–202.
13. Angelova MI, Dimitrov DS (1986) Liposome electroformation. *Faraday Discuss Chem Soc* 81:303–311.
14. Angelova M, Dimitrov D (1988) A mechanism of liposome electroformation. *Trends in Colloid and Interface Science II*, ed Degiorgio V (Springer, Berlin), pp 59–67.
15. Angelova M (2000) *Giant vesicles. Perspectives in Supramolecular Chemistry*, eds Luisi PL, Walde P (Wiley-Interscience Chichester, UK), 1st Ed, pp 27–36.
16. Aisenbrey C, Bertani P, Bechinger B (2010) Solid-state NMR investigations of membrane-associated antimicrobial peptides. *Methods Mol Biol* 618:209–233.
17. Aisenbrey C, Michalek M, Salnikov E, Bechinger B (2013) *Lipid-Protein Interactions: Methods and Protocols (Methods in Molecular Biology)*, ed Jh K (Springer, New York).
18. Salnikov ES, et al. (2011) Structure and alignment of the membrane-associated antimicrobial peptide arenicin by oriented solid-state NMR spectroscopy. *Biochemistry* 50(18):3784–3795.
19. Aisenbrey C, Bechinger B (2004) Tilt and rotational pitch angle of membrane-inserted polypeptides from combined 15N and 2H solid-state NMR spectroscopy. *Biochemistry* 43(32):10502–10512.
20. Bechinger B, Salnikov ES (2012) The membrane interactions of antimicrobial peptides revealed by solid-state NMR spectroscopy. *Chem Phys Lipids* 165(3):282–301.
21. Salnikov E, Bertani P, Raap J, Bechinger B (2009) Analysis of the amide (15)N chemical shift tensor of the C(α) tetrasubstituted constituent of membrane-active peptaibols, the α-aminoisobutyric acid residue, compared to those of di- and tri-substituted proteinogenic amino acid residues. *J Biomol NMR* 45(4):373–387.
22. Batchelder LS, Niu CH, Torchia DA (1983) Methyl reorientation in polycrystalline amino acids and peptides: A deuteron NMR spin-lattice relaxation study. *J Am Chem Soc* 105:2228–2231.
23. Strandberg E, Esteban-Martín S, Salgado J, Ulrich AS (2009) Orientation and dynamics of peptides in membranes calculated from 2H-NMR data. *Biophys J* 96(8):3223–3232.
24. Michalek M, Salnikov ES, Werten S, Bechinger B (2013) Membrane interactions of the amphipathic amino-terminus of huntingtin. *Biochemistry* 52(5):847–858.
25. Berendsen HJC, van der Spoel D, van Drunen R (1995) GROMACS: A message-passing parallel molecular dynamics implementation. *Comput Phys Commun* 91:43–56.
26. Hess B, Kutzner C, van der Spoel D, Lindahl E (2008) GROMACS 4: Algorithms for highly efficient, load-balanced, and scalable molecular simulation. *J Chem Theory Comput* 4:435–447.
27. Klauda JB, et al. (2010) Update of the CHARMM all-atom additive force field for lipids: Validation on six lipid types. *J Phys Chem B* 114(23):7830–7843.
28. Bussi G, Donadio D, Parrinello M (2007) Canonical sampling through velocity rescaling. *J Chem Phys* 126(1):014101.
29. Darden T, York D, Pedersen L (1993) Particle mesh Ewald: An N· log (N) method for Ewald sums in large systems. *J Chem Phys* 98:10089.
30. Essmann U, et al. (1995) A smooth particle mesh Ewald method. *J Chem Phys* 103: 8577–8593.
31. Hess B, Bekker H, Berendsen HJC, Fraaije JGEM (1997) LINCS: A linear constraint solver for molecular simulations. *J Comput Chem* 18:1463–1472.
32. Feenstra KA, Hess B, Berendsen HJC (1999) Improving efficiency of large time-scale molecular dynamics simulations of hydrogen-rich systems. *J Comput Chem* 20:786–798.
33. Murzyn K, Róg T, Pasenkiewicz-Gierula M (2005) Phosphatidylethanolamine-phosphatidylglycerol bilayer as a model of the inner bacterial membrane. *Biophys J* 88(2):1091–1103.
34. Jo S, Kim T, Iyer VG, Im W (2008) CHARMM-GUI: A web-based graphical user interface for CHARMM. *J Comput Chem* 29(11):1859–1865.
35. Jorgensen WL, Chandrasekhar J, Madura JD, Impey RW, Klein ML (1983) Comparison of simple potential functions for simulating liquid water. *J Chem Phys* 79:926–935.
36. Berendsen HJC, Postma JPM, Van Gunsteren WF, DiNola A, Haak JR (1984) Molecular dynamics with coupling to an external bath. *J Chem Phys* 81:3684–3690.
37. Wolf MG, Hoefling M, Aponte-Santamaría C, Grubmüller H, Groenhof G (2010) g_membed: Efficient insertion of a membrane protein into an equilibrated lipid bilayer with minimal perturbation. *J Comput Chem* 31(11):2169–2174.
38. Kutzner C, Grubmüller H, de Groot BL, Zachariae U (2011) Computational electrophysiology: The molecular dynamics of ion channel permeation and selectivity in atomistic detail. *Biophys J* 101(4):809–817.
39. Hille B (2001) *Ion channels of excitable membranes* (Sinauer, Sunderland, MA), 3rd Ed.
40. Pierce B, Tong W, Weng Z (2005) M-ZDOCK: A grid-based approach for Cn symmetric multimer docking. *Bioinformatics* 21(8):1472–1478.

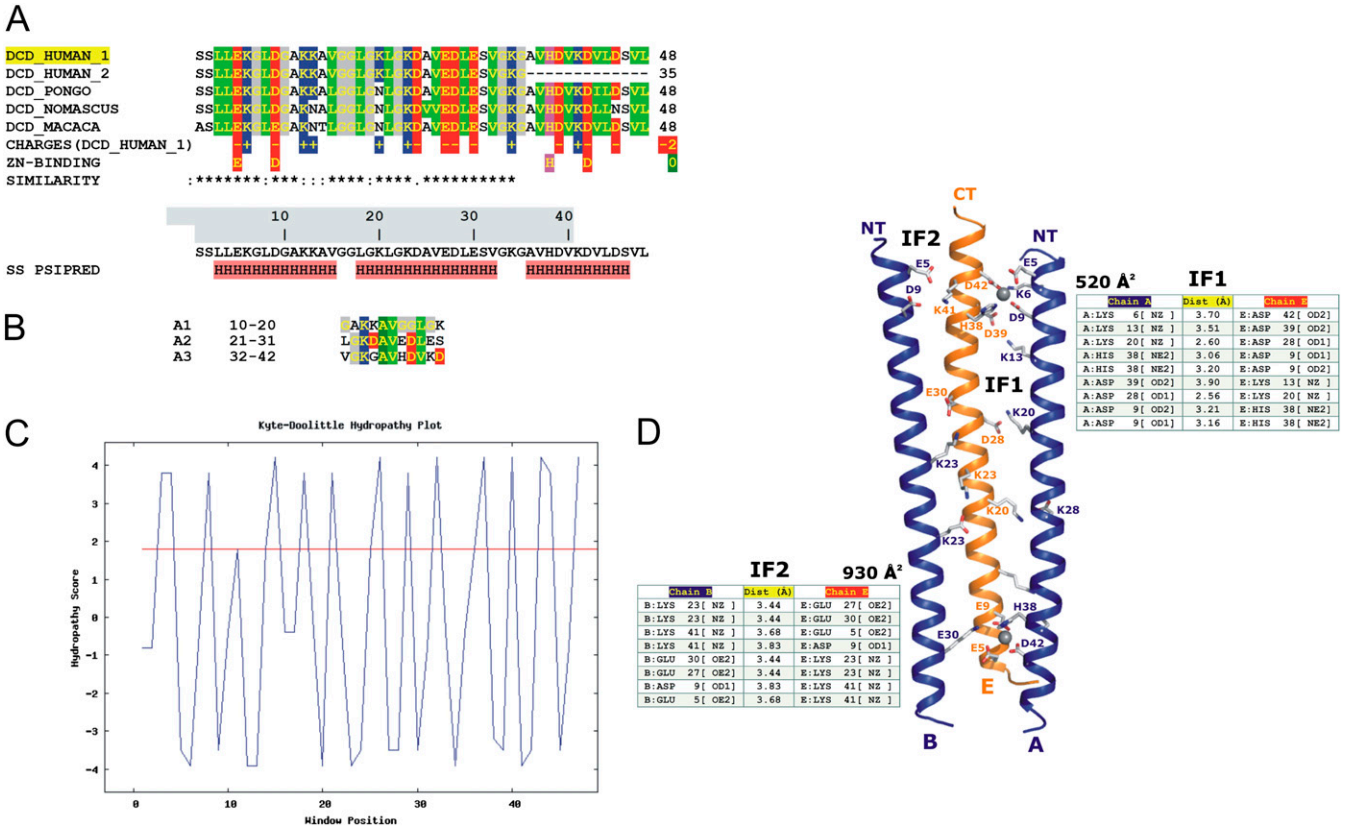

Fig. S1. Sequence and structural analysis of human DCD. (*A*) Sequence alignment of human DCD (isoform 1) and sequences deposited to the current EXPASY sequence database (www.expasy.org). Four sequences similar to DCD were extracted with a PSI-BLAST search, one of which is a second human isoform, and the remaining three sequences are derived from monkey genomes. Hydrophobic residues are colored in green, positively charged residues are blue, and negatively charged residues are red. Residues involved in Zn binding are marked and the similarity between the sequences chosen is represented by (*) for identical residues and (:) for similar residues. In addition, the secondary structure as predicted by PSIPRED is shown. (*B*) Analysis of the sequence for repetitive elements. The peptides show three of those elements (residue numbers are provided). (*C*) Amphipathic plot of the DCD peptide with Kyte–Doolittle values. (*D*) Analysis of the two peptide interfaces. Each peptide in the hexameric DCD structure faces two differently oriented peptide neighbors. Therefore, two different interfaces are formed, which are analyzed here with the PISA server software (http://www.ebi.ac.uk/msd-srv/prot_int/pistart.html). The size of the interfaces is given in Ångstrom and the residues important for interface stabilization are mentioned together with the residue numbers and distances.

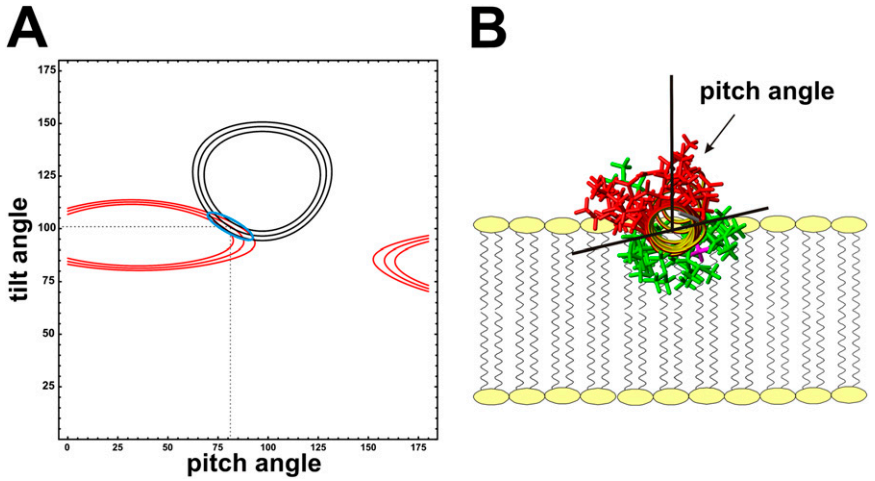

Fig. S2. ss-NMR helix tilt/pitch angles. (*A*) The tilt/pitch angular pairs that agree with the ^{15}N chemical shift and the ^{2}H quadrupolar splitting observed in oriented POPE/POPG 3/1 (including error bars) are shown by the red and black traces, respectively. (*B*) The energetically most probable alignment is schematically illustrated. Neutral Leu, Val are colored in green, charged Lys, Glu and Asp in red, and Ala25 is in magenta.

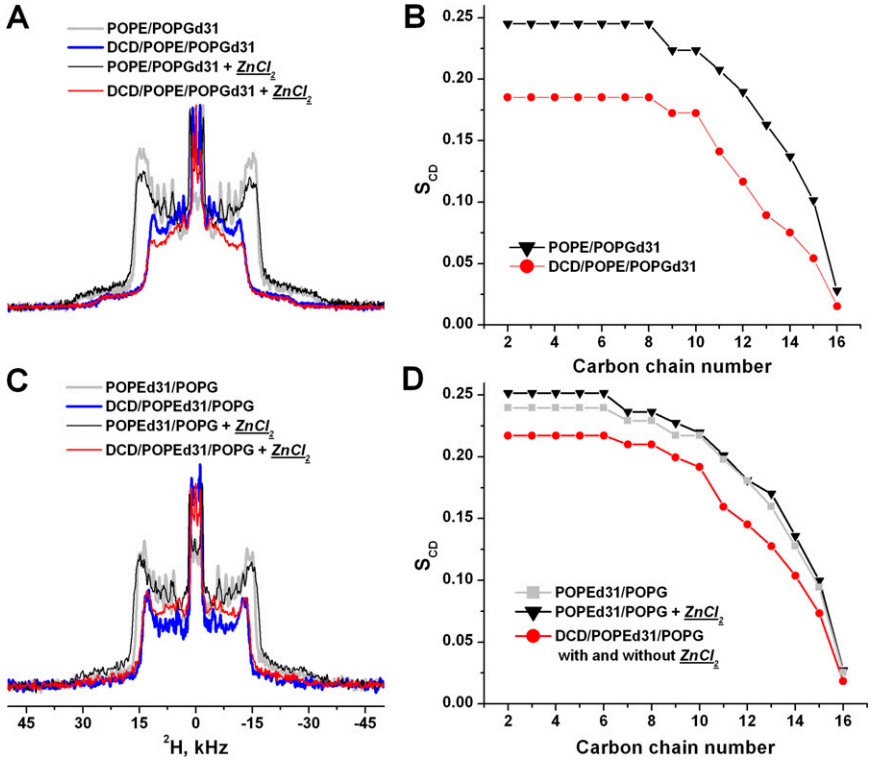

Fig. S3. ^{2}H ss-NMR spectra and order parameters of ^{2}H-chain deuterated lipid membranes. (*A* and *C*) ^{2}H solid-state NMR spectra of ^{2}H-chain deuterated lipid membranes and (*B* and *D*) the corresponding deuterium order parameters. The spectra are recorded at 310 K from nonoriented and fully hydrated POPE/POPG 3:1 mol/mole membranes where the palmitoyl chains of either POPG (*A* and *C*) or POPE (*B* and *D*) are fully deuterated. In gray (squares) are shown the lipids alone, in black (inverted triangles) the pure lipids in the presence of $ZnCl_2$. The data in the presence of 2 mol % DCD are shown in blue and red (circles) in the absence and presence of zinc, respectively. The data with and without $ZnCl_2$ overlap in *B* as well as in *D* for the DCD/POPE/POPG mixtures.

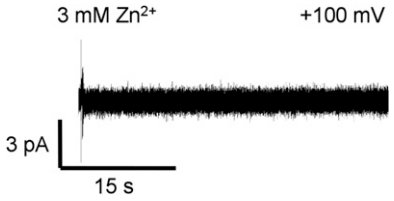

Fig. S4. Electrophysiological measurements on the DCD mutant H38A. Even under addition of zinc ions, no specific current steps are observed.

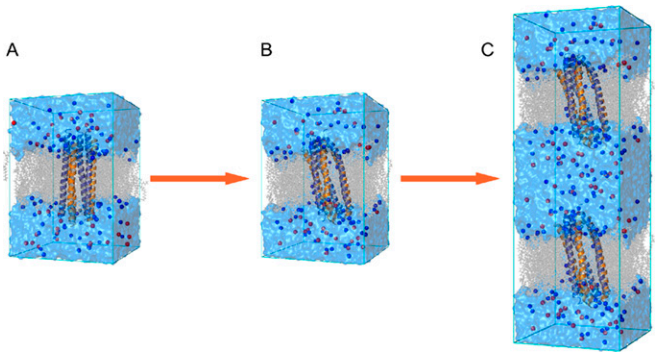

Fig. S5. Model system used in the MD simulations. (*A*) The initial simulation system, which contains the X-ray structure of DCD (orange and deep blue cartoon helices), the POPE/POPG (3:1) lipids bilayer (gray sticks), water box (light blue surface), Na^+ (blue spheres), and Cl^- (red spheres) ions. (*B*) The MD conformation after 100-ns simulation, which was then duplicated in the membrane normal direction to form the double-patch simulation system for the computational electrophysiology simulations (*C*).

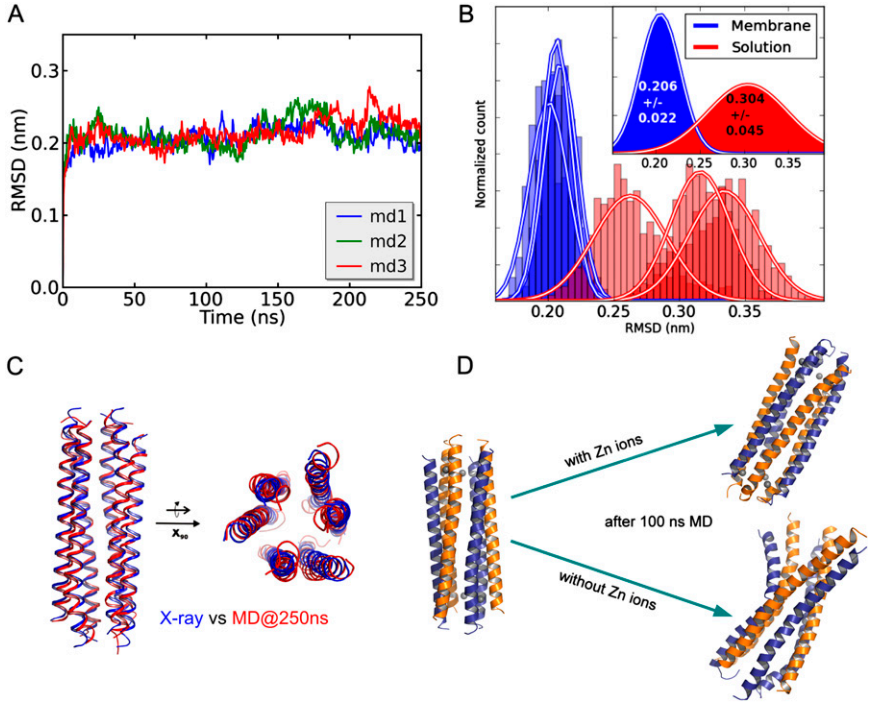

Fig. S6. Stability of the X-ray structure in MD simulations. (*A*) Evolution of the RMSD of the DCD oligomer (alpha carbon atoms) in the POPE/POPG bilayer during the 250-ns MD simulations. Results are calculated from three independent simulations. (*B*) Comparison of the stability of the DCD X-ray structure in membrane (blue) and solution (red). On average, the oligomer structure deviates from the X-ray structure by about 1 Å more in solution than in the membrane. Therefore, the X-ray channel structure is relatively more stable in a membrane environment. (*C*) Side and top views of the comparison between the X-ray structure (in blue) and the MD conformation at 250 ns (in red), respectively. The MD conformation was fitted onto the X-ray structure, which was then used as the starting structure for additional computational electrophysiology simulations. (*D*) Importance of Zn^{2+} ions for the stability of the oligomer channel. Starting with the initial oligomer structure in the single-patch MD simulations, the channel structure is preserved in the MD simulations in the presence of six Zn^{2+} ions. By contrast the channel structure evolves strong distortions in the absence of Zn^{2+}.

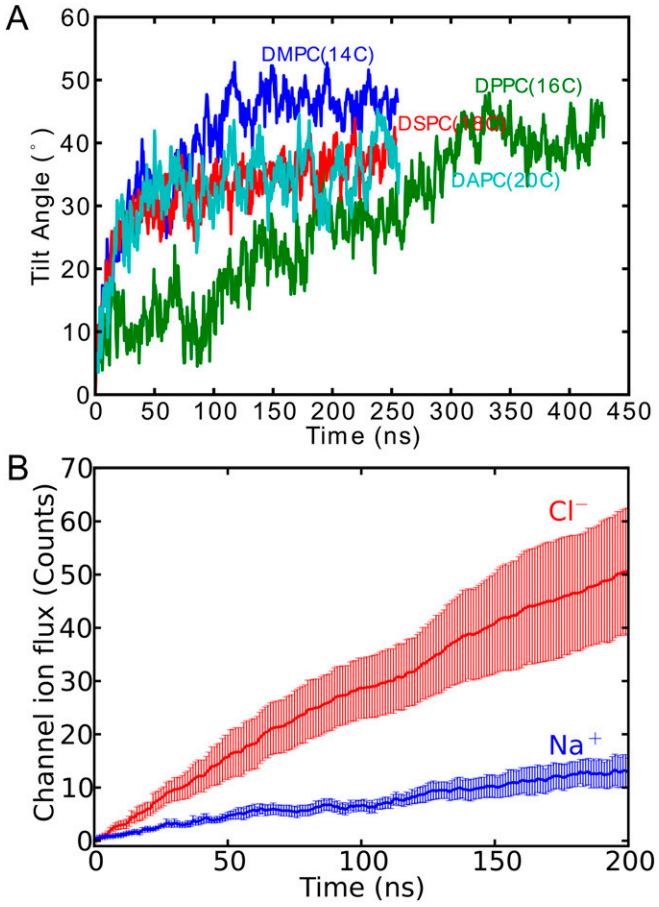

Fig. S7. Additional simulation results. (*A*) Evolution of the tilt angle of the DCD channel in various lipid bilayers in MD simulations. The simulations were performed in an NPT ensemble at a temperature of 345 K to keep all lipids in their fluid phase. As can be seen with the increase of the lipid tail length, i.e., the thickness of the bilayer, the tilt angle of the DCD channel decreases. In DPPC, the tilting process occurs on a much longer time scale than in the other lipid bilayers. Therefore, the type of the lipid bilayer and its composition may have a significant effect on the channel properties, which we reserve for a future study. (*B*) Exemplary ion permeation counts during the 200-ns computational electrophysiology simulations (averages from six independent simulations with SEs), with 0.15 M NaCl in solution.

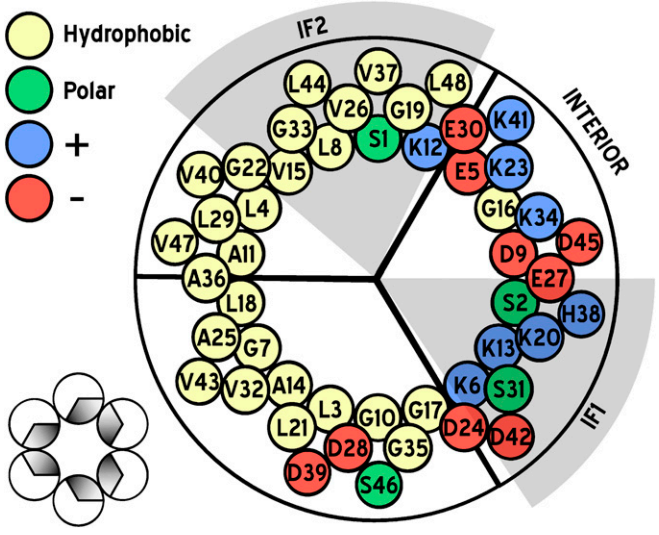

Fig. S8. Helical wheel analysis of a monomer of DCD. Top view of a monomeric helical wheel, showing the distribution of residues and their types. Angular partitions of hydrophobic/hydrophilic regions are distinctly centered around 240°/120°, favoring hexamer formation when being embedded in a lipid bilayer, as shown (*Lower Left*) where the gray shaded areas indicate the hydrophilic surfaces and interfaces.

Table S1. Data collection and refinement statistics

	Dermcidin*
Data collection	
Space group	C2
Cell dimensions	
a, *b*, *c* (Å)	76.35, 50.72, 45.73
α, β, γ (°)	90, 117.74, 90
Resolution (Å)	33–2.5 (2.66–2.5)
R_{merge}	0.02 (0.51)
$I/\sigma I$	17 (2.95)
Completeness (%)	98.8 (96.8)
Redundancy	7.2 (7.1)
Wavelength	1.2795
Refinement	
Resolution (Å)	33–2.5 (2.56–2.5)
No. reflections	5189
R_{work}/R_{free}	0.21/0.27 (0.23/0.27)
No. atoms (all)	
Protein	980
Ions (Zn^{2+})	6
Water	20
B factors	
Protein	27.7
Ions (Zn^{2+})	70.5
Water	31.7
Root-mean square. deviations	
Bond lengths (Å)	0.02
Bond angles (°)	2.0

*Values in parentheses are for highest-resolution shell.

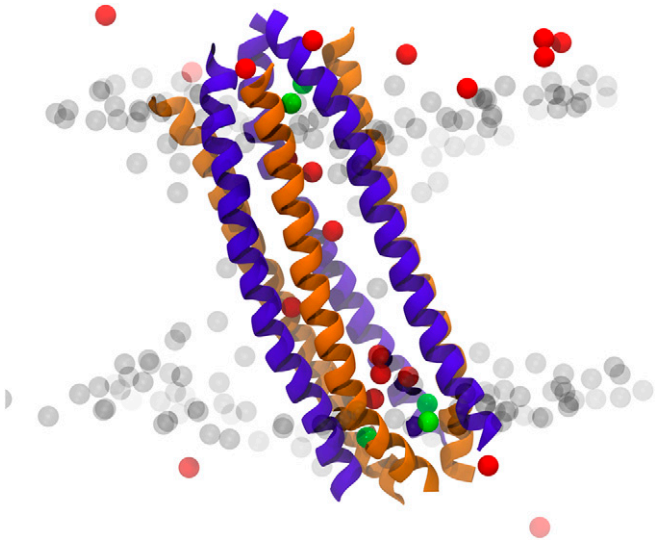

Movie S1. Multiion permeation mechanism across DCD driven by transmembrane electric fields present across bacterial membranes. Ions enter sideways into the pore across the lateral openings that occur at the trimeric interfaces. Anion transfer across the inner pore usually involves single ion "hopping" steps. Near the channel exit, anions accumulate to form a cluster of three to four ions. Ions exiting the channel are often observed to be translocated by multiion "knock-on" effects, by which anions are transferred to the bulk solution.

Movie S1

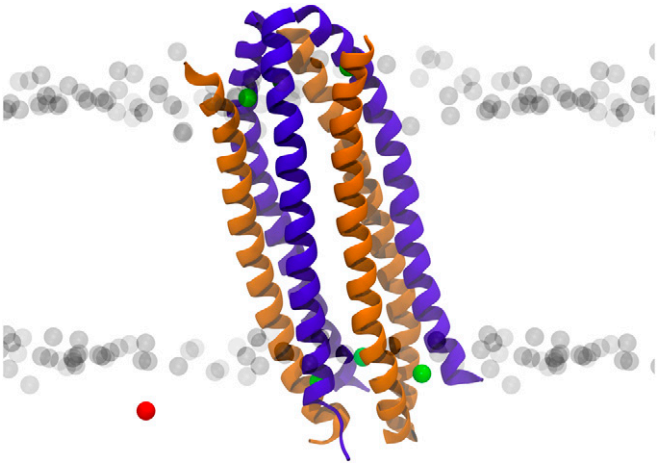

Movie S2. Single anion followed on its pathway through the DCD channel, driven by a transmembrane electric field. Simulations settings are identical to Movie S1, but only one permeating ion is shown to clearly illustrate the permeation pathway.

Movie S2